

VIP Very Important Paper

Special Collection



www.batteries-supercaps.org

Importance of Mass Transport in High Energy Density Lithium-Sulfur Batteries Under Lean Electrolyte Conditions

Shanglin Li,^[a] Shota Ishikawa,^[c] Jiali Liu,^[b] Kazuhide Ueno,^[a, b] Kaoru Dokko,^[a, b] Gen Inoue,*^[c] and Masayoshi Watanabe*^[b]

The operation of a lithium-sulfur (Li–S) battery under lean electrolyte conditions is essential for enhancing the energy density to a practical level. It is rather challenging to reduce the amount of electrolyte in Li–S cells because the discharge reactions of sulfur (Li_2S_x formation: $x=8-1$) occur via a fully dissolution/precipitation conversion mechanism in conventional electrolyte solutions. Therefore, the use of sparingly solvating electrolytes has been reported as an effective method to reduce the electrolyte content in Li–S cells. However, the majority of related research to date has been based on the use of an excess amount of electrolyte and low S loading. In this study, we investigated the performance of Li–S cells using cathodes with a relatively high S loading ($>4 \text{ mg cm}^{-2}$) under lean electrolyte

conditions of sparingly solvating electrolytes. The products of inhomogeneous discharge reactions occurring at the separator side in the Li–S cell cathodes blocked the void spaces of the cathode, and the porosity of the cathode decreased due to the expansion of the active material. In addition, the ion pathway toward the interior parts of the electrode (close to the current collector) was hindered, and further discharge reactions were inhibited. The inhomogeneous discharge reactions could be alleviated by enhancing the transport properties of the electrolyte and adequately maintaining the porous structure of the cathode by incorporating an additive in it. The effects of these changes on the Li–S cell performance were also further confirmed by numerical simulations.

Introduction

The demand for rechargeable batteries with high energy densities, long-term cycling performances, and reduced costs is growing rapidly for achieving long driving ranges and stable service lives of electric vehicles and stationary renewable energy storage devices.^[1–4] However, conventional lithium-ion batteries (LIBs) based on Li-ion intercalation chemistry, which have been widely applied in portable devices, cannot satisfy the demand for energy densities exceeding 250 Wh kg^{-1} .^[5,6] Therefore, lithium-sulfur (Li–S) batteries have attracted attention as next-generation rechargeable secondary batteries owing to their

extremely high theoretical energy densities (2600 Wh kg^{-1}), which rely on the high capacity of elemental sulfur (1672 mAh g^{-1}). In addition, the natural abundance and low cost of sulfur render it a promising active material of cathode for practical applications.^[7,8] However, several obstacles continue to hinder the practical application of Li–S batteries, including the insulating nature of elemental sulfur and its electrochemically reduced products (Li_2S_x : $x=8-1$), the large volumetric expansion of S_8 by 1.8 times upon its full lithiation to Li_2S , and the dissolution of lithium polysulfides (Li_2S_x , especially for $x=8-4$) into electrolytes during the discharge/charge processes.^[9–12]

Typically, conventional organic electrolyte solutions for Li–S batteries, i.e., 1 M lithium bis(trifluoromethanesulfonyl)amide, $\text{Li}[\text{N}(\text{SO}_2\text{CF}_3)_2]$ (abbreviated as $\text{Li}[\text{NTf}_2]$), dissolved in a 1:1 mixture of 1,2-dimethoxyethane and 1,3-dioxolane (DME/DOL), causes the severe dissolution of Li_2S_x from the sulfur cathode and leads to a redox shuttle phenomenon, leading to a rapid capacity decay, low Coulombic efficiency, and self-discharge behaviour. In addition, it is difficult to reduce the amount of electrolyte required for Li–S cells (i.e., electrolyte/sulfur (E/S) ratio, $\mu\text{L}_{\text{electrolyte}}/\text{mg}_{\text{sulfur}}$) using this kind of polysulfide-solubilising electrolyte because of the catholyte nature of the dissolved Li_2S_x , which requires enough electrolyte to ensure smooth dissolution/precipitation reaction pathways. The operation of Li–S batteries with a low E/S ratio result in high polysulfide concentrations, leading to significantly sluggish Li_2S electrodeposition.^[13] Therefore, severe polarisation and capacity degradation occur with a reduction in the E/S ratio.^[14] However, a low E/S ratio is essential to achieve a high energy density at a cell level that is compatible with the current lithium-ion technologies.^[15,16]

[a] S. Li, Prof. K. Ueno, Prof. K. Dokko
Department of Chemistry and Life Science
Yokohama National University
79-5 Tokiwadai, Hodogaya-ku,
Yokohama 240-8501, Japan

[b] Dr. J. Liu, Prof. K. Ueno, Prof. K. Dokko, Prof. M. Watanabe
Advanced Chemical Energy Research Center,
Institute of Advanced Sciences
Yokohama National University
79-5 Tokiwadai, Hodogaya-ku,
Yokohama 240-8501, Japan
E-mail: mwatanab@ynu.ac.jp

[c] S. Ishikawa, Prof. G. Inoue
Department of Chemical Engineering,
Faculty of Engineering
Kyushu University
744 Motooka, Nishi-ku,
Fukuoka 819-0395, Japan
E-mail: ginoue@chem-eng.kyushu-u.ac.jp

Supporting information for this article is available on the WWW under
<https://doi.org/10.1002/batt.202100409>

An invited contribution to a Special Collection dedicated to Lithium-Sulfur Batteries.

Considering the afore-mentioned issues associated with the use of polysulfide (Li_2S_x)-solubilising electrolytes, sparingly solvating electrolytes have been proposed as promising alternatives for Li–S cells.^[17,18] The thermodynamic suppression of polysulfide dissolution has been accomplished in weakly coordinating electrolyte solutions, such as ionic-liquid-based electrolytes,^[19–21] highly concentrated electrolytes,^[22,23] and fluoroether-based electrolytes.^[24–27] In our previous work, we reported that an equimolar mixture of tetraglyme (G4) and $\text{Li}[\text{NTf}_2]$, i.e., $[\text{Li}(\text{G4})_2]\text{[NTf}_2]$, classified as a solvate ionic liquid, inhibits polysulfide dissolution to a large extent.^[28] Moreover, the addition of 1,1,2,2-tetrafluoroethyl 2,2,3,3-tetrafluoropropyl ether (HFE) to $[\text{Li}(\text{G4})_2]\text{[NTf}_2]$ resulted in a further lower polysulfide solubility and enhanced ionic conductivity, leading to a higher capacity with high Coulombic efficiency.^[29] We also found that a concentrated solution of $\text{Li}[\text{NTf}_2]$ in sulfolane (SL), i.e., $[\text{Li}(\text{SL})_2]\text{[NTf}_2]$, exhibits a high Li^+ transference number owing to the high diffusivity of Li^+ in the electrolyte, which is attributable to the hopping conduction of Li^+ by the ligand-exchange mechanism between SL and $[\text{NTf}_2]^-$.^[30,31] In addition, Kaskel et al. reported that an electrolyte solution consisting of an SL/HFE mixture with 1.5 M $\text{Li}[\text{NTf}_2]$ exhibits a low polysulfide solubility, and thus enables a high discharge capacity and high Coulombic efficiency at the pouch cell level, particularly when a low electrolyte amount is employed.^[32,33] We also reported that the $[\text{Li}(\text{SL})_2]\text{[NTf}_2]$ electrolyte with or without HFE added as a diluent has a particularly low solubility for polysulfide and facilitates superior rate capability than the $[\text{Li}(\text{G4})_2]\text{[NTf}_2]$ system.^[30] Although the above-mentioned sparingly solvating electrolytes are attractive for reducing the E/S ratio in Li–S batteries, a high sulfur loading is also recognised as an essential factor that can enhance the energy density.^[34] However, to date, there have been very few reports on the usage of sparingly solvating electrolytes along with a relatively high sulfur loading in the cathode to achieve a low E/S ratio, and thus realise a high energy density at the practical cell level.^[32,35] Our previous study proposed a commercially available black pigment, titanium black (TiB), as a multifunctional additive for sulfur cathodes.^[36] The amphiphilic nature of TiB enabled a homogeneous and thick coating of the electrode on a current collector ($>4 \text{ mg cm}^{-2}$), and led to improved electrode wettability by the electrolyte.^[36] Consequently, a pouch cell with an extremely low E/S ratio of 3.2 was successfully fabricated using an SL-based electrolyte to achieve a high energy density of 280 Wh kg^{-1} .^[36]

In this context, herein, we discuss the importance of mass transport within the cathode based on the charge/discharge results of pouch cells consisting of a cathode with a relatively high sulfur loading ($>4 \text{ mg cm}^{-2}$) under lean electrolyte conditions. Initially, by employing a sparingly solvating G4-based electrolyte with a low Li^+ transport capability, we demonstrate that the actual mass transport in a Li–S cell is not only determined by the intrinsic properties of the electrolyte itself, but also by the properties of the sulfur cathode. In addition, we demonstrate the TiB additive-induced enhancement of the mass transport in the sulfur cathode using a sparingly solvating SL-based electrolyte with a high Li^+ transport capability. This effect was also confirmed by numerical simulations. Finally, pouch-type

Li–S batteries were fabricated and their energy densities were evaluated. Ultimately, the aim of this study is to clarify the key factors that influence the performance of a Li–S battery consisting of a cathode with a high sulfur loading under lean electrolyte conditions.

Results and Discussion

Inhomogeneous reaction in the sulfur cathode

To achieve high energy density Li–S batteries, both a relatively high sulfur content and lean electrolyte conditions (low E/S) are essential.^[34] Owing to the unique nature of the Li–S chemistry,^[37] to the best of our knowledge, the lowest E/S that can be achieved is $\sim 3 \mu\text{L mg}^{-1}$,^[38,39] unlike in the case of commercial LIBs. Therefore, based on our calculations (see Figure 1), to achieve a high energy density ($>350 \text{ Wh kg}^{-1}$), a cathode sulfur loading of $>4.0 \text{ mg cm}^{-2}$ is the basic requirement. Considering the large “dead volume” fraction in a coin cell, in our discussion based on the preliminary screening of coin cells,^[40] we defined electrolyte volumes of 80 and 110 μL as lean and sufficient electrolyte conditions, respectively.

Initially, according to our previous study,^[35] we selected $[\text{Li}(\text{G4})_{0.8}]\text{[NTf}_2]$ + 4.3HFE as the sparingly solvating electrolyte for Li_2S_x with a low Li-ion transport capability. As shown in Figure S1 (Supporting Information), high discharge capacities of 1193 and 1041 mAh g^{-1} could be obtained with the use of a thinner S_8/KB cathode (3.2 mg cm^{-2}) and under sufficient electrolyte conditions (110 μL), respectively. However, as indicated by the red curve in Figure 2(a), under lean electrolyte conditions, the cell containing the TiB-free cathode exhibited a particularly low discharge capacity (138 mAh g^{-1}) with the complete disappearance of the second discharge plateau, which significantly contributes to the

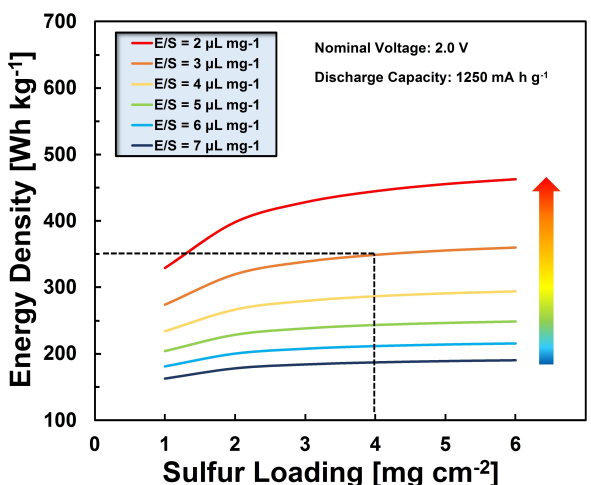


Figure 1. Calculated energy density of a Li–S battery as a function of sulfur loading under different E/S conditions. The total cell weight was calculated from the weights of the cathode (composite cathode containing 70 wt% S_8 + Al current collector), anode (theoretical weight of Li metal), separator (Celgard 3501), and electrolyte ($\rho = 1.55 \text{ g mL}^{-1}$), excluding the weights of the Al laminate film package and tabs.

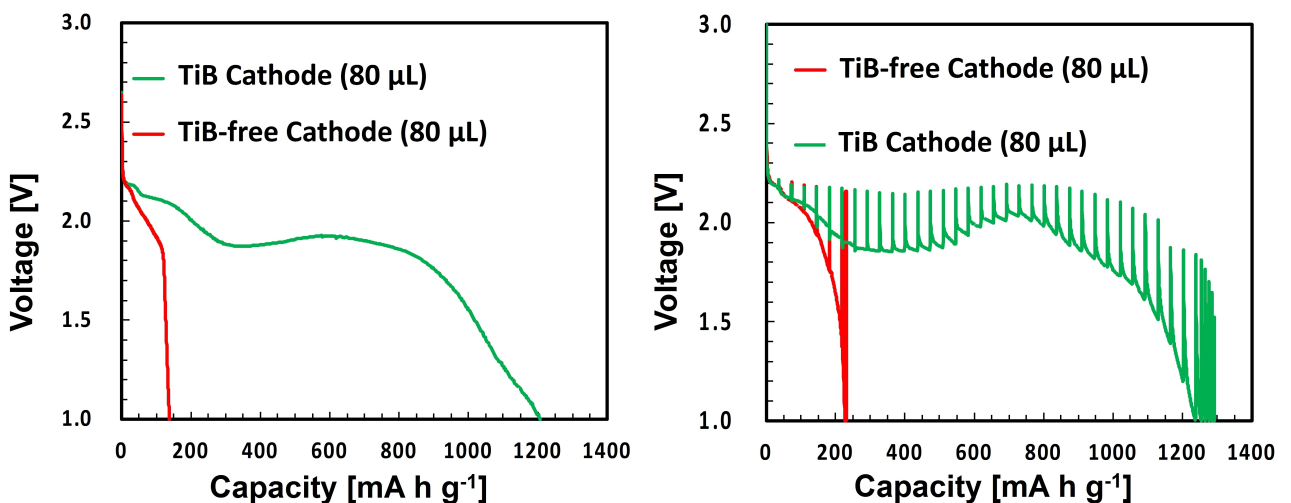


Figure 2. a) Initial discharge curves using $[\text{Li}(\text{G4})_{0.8}][\text{NTf}_2] + 4.3\text{HFE}$ at $150 \mu\text{A cm}^{-2}$ for TiB-free (S loading: 4.2 mg cm^{-2}) and TiB-added (S loading: 4.2 mg cm^{-2}) cathodes under lean electrolyte conditions ($80 \mu\text{L}$), and b) GITT measurements for both electrodes.

capacity delivery. In Li_2S_x -solvilising electrolytes, it is speculated that a large amount of electrolyte easily results in a highly concentrated polysulfide catholyte situation during the initial discharge plateau, causing sluggish Li_2S electrochemical deposition, and thus severe polarisation of the cell and an early arrival at the cut-off voltage.^[13] However, according to our previous study, the saturation concentration of the most-soluble polysulfide (Li_2S_8) in the G4-based electrolyte used in this study, $[\text{Li}(\text{G4})_{0.8}][\text{NTf}_2] + 4.3\text{HFE}$, is as low as 1 mM_S ,^[35] and the saturation concentrations of lower-chain-length Li_2S_x compounds, such as Li_2S_6 and Li_2S_4 , are much lower than that of Li_2S_8 .^[29] Hence, the above rationalisation of the low discharge capacity is not valid in this case. In the presence of a sparingly solvating electrolyte, the conversion of molecular sulfur to Li_2S primarily occurs in the solid phase, which is in significant contrast to a full dissolution and precipitation pathway of sulfur to Li_2S conversion in an electrolyte consisting of $1 \text{ M Li}[\text{NTf}_2]$ in DME/DOL with much higher polysulfide solubility (Li_2S_8 solubility: 6600 mM_S).^[35] One possible reason for the low discharge capacity could be the actual mass transport occurring inside the cathode.^[30] When an electrolyte with a low Li-ion transport capability is used under lean electrolyte conditions, the Li-ion transport inside the cathode lags behind the cathode reduction reactions. The poor wettability of the TiB-free electrode to the electrolyte may also hinder the Li-ion transport capability. In contrast, TiB included as a multifunctional sulfur cathode additive enabled the fabrication of crack-free highly S-loaded porous electrodes with a high wettability to the electrolyte.^[36] To evaluate how these features affect the mass transport occurring within the sulfur cathode, we also examined the performance of the TiB-added electrode under the same lean conditions using the G4 electrolyte. As shown by the green curve in Figure 2(a), the TiB-added electrode exhibited a high discharge capacity of 1207 mAh g^{-1} even under the lean electrolyte condition. The galvanostatic intermittent titration technique (GITT) measurements (Figure 2(b)) further indicated that the overpotential of the

cell containing the TiB-free cathode increased continuously during the discharge process, and that the cell potential reached 1.0 V at 230 mAh g^{-1} capacity, consistent with the low discharge capacity demonstrated in Figure 2(a). Remarkably, the addition of TiB alleviated the continuous increment of the overpotential, and the cell potential reached 1.0 V at a significantly higher capacity of 1230 mAh g^{-1} .

To understand the cause of the continuous increase in overpotential for the TiB-free cathode and to determine how the TiB additive facilitated a high discharge capacity, the Li-S coin cells were disassembled at a specific depth of discharge (Figure S2), and the sulfur cathodes were investigated by scanning electron microscopy (SEM) combined with energy dispersive X-ray spectroscopy (EDX) to analyse their structure and sulfur distribution, respectively. Figure 3 displays representative high-magnification SEM images of the cathodes, while Figure S3 shows the corresponding low-magnification SEM images for larger sample areas. As shown in Figure 3, compared with the surface morphology of the fresh TiB-free cathode before discharge, a loss of porosity is apparent after discharge for both types of cathodes, irrespective of the addition of TiB, because of the volumetric expansion occurring during the lithiation of sulfur species.^[10] In particular, the loss of the porous structure appeared to be more significant for the TiB-free cathode (Figures 3a and c) than for the TiB-added one (Figures 3b and d). Note that SEM images can only reflect the local morphologies at the scale of several micrometres. However, we investigated large areas of each sulfur cathode to confirm the differences between different electrodes. Further, the same features were observed consistently to replicate samples processed under equivalent conditions. Therefore, we infer that the morphological differences observed in the SEM images are possibly related to the different overpotentials of the cathodes during the discharge process (i.e., the lithiation of sulfur). For the discharge reactions (i.e., the reduction of sulfur) to occur smoothly, Li-ion transport inside the cathode is

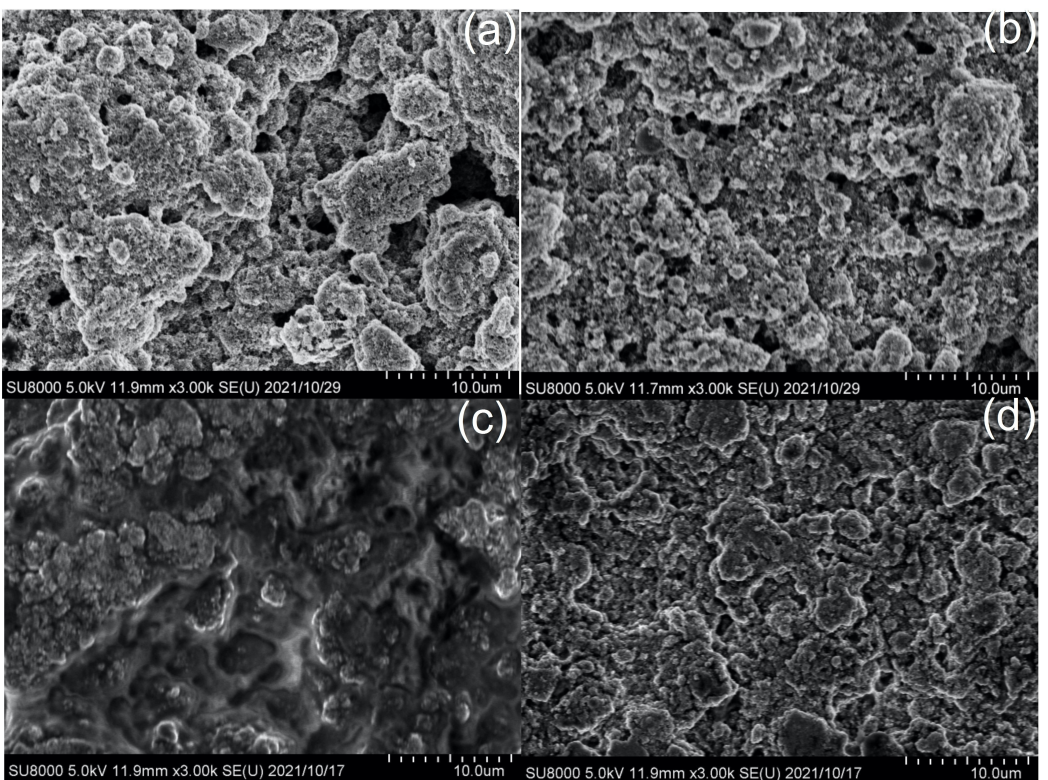


Figure 3. SEM surface morphologies of fresh cathodes (before discharge), i.e., a) TiB-free cathode and b) TiB-added cathode, compared with those of the cathodes discharged up to 250 mAh g^{-1} in $[\text{Li(G4)}_{0.8}][\text{NTf}_2] + 4.3\text{HFE}$: c) TiB-free cathode and d) the TiB-added cathode.

essential to compensate for the negative charge of the discharged products (S_x^{2-} : $x=8-1$; x decreases from a larger number to a smaller one). Therefore, the blockage of the porous cathode structure would hinder Li-ion transport inside the cathode. It is also worth mentioning that the discharge reaction did not proceed homogeneously inside the cathode but began at the surface and progressed inward. This tendency was more apparent for the TiB-free cathode. Figure 4 shows surface SEM images combined with the EDX sulfur mapping results for the TiB-free and TiB-added cathodes discharged up

to 250 mAh g^{-1} . On the surface of the TiB-free cathode, large crystal-like sulfur-rich particles accumulated over a background with homogeneous sulfur distribution. These large particles are possibly the final lithiation products of the sulfur species, Li_2S_x , and indicate that the discharge reactions were mainly concentrated on the surface of the TiB-free cathode. In contrast, a surface with homogeneous distribution of sulfur was observed for the TiB-added cathode, suggesting that discharge reactions were not restricted to the outer surface.

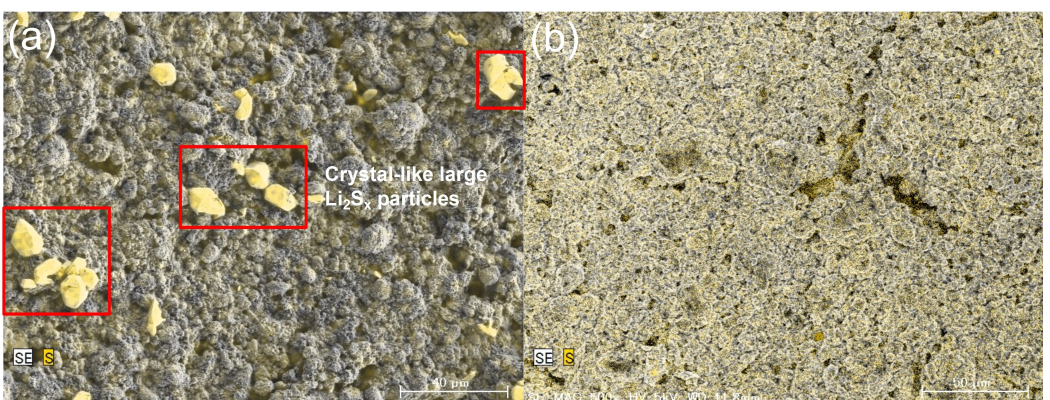


Figure 4. Surface morphology observed by SEM combined with EDX mapping of sulfur for a) TiB-free and b) TiB-added cathodes discharged up to 250 mAh g^{-1} in $[\text{Li(G4)}_{0.8}][\text{NTf}_2] + 4.3\text{HFE}$.

To further examine the morphological changes in the cathodes, cross-sectional images of the sulfur cathodes at the same discharge depth (250 mAh g^{-1}) were also obtained (Figure S4). The images clearly indicated that the porosity loss of the TiB-free cathode was severe at the surface (i.e., close to the separator), while the porosity was maintained in the deeper regions (i.e., close to the Al current collector). This indicates that under high sulfur loading and lean electrolyte conditions, the electrochemical reactions of the TiB-free cathode are limited by the transport of Li ions. Furthermore, the closure of pores on the surface of the sulfur cathode due to the volume expansion owing to S_8 to Li_2S_x conversion possibly results in the blockage of the ion pathway, and thus, the reaction cannot proceed smoothly in the deeper regions of the cathode. This leads to a low discharge capacity and a continuous increase in the overpotential during the discharge process (Figure 2). In contrast, for the TiB-added cathode, the porosity was maintained at a relatively good level throughout the electrode, from the surface to deeper regions, indicating that the discharge reactions possibly occurred more homogeneously along the thickness direction of the electrode. This could be attributed to the fabrication of a crack-free porous electrode and the improvement of its wettability to the electrolyte, which was enabled by the TiB additive.

Effect of the electrolyte properties on the Li–S cell performance

Our previous study also revealed that $[\text{Li}(\text{SL})_2][\text{NTf}_2]$ diluted with HFE (i.e., $[\text{Li}(\text{SL})_2][\text{NTf}_2] + 4.0\text{HFE}$) has a low polysulfide solubility (Li_2S_8 solubility: 1 mM_S ^[30]) comparable to that of $[\text{Li}(\text{G4})_{0.8}][\text{NTf}_2] + 4.3\text{HFE}$, and that the Li–S cells using a cathode with a low sulfur content (e.g., $\sim 1 \text{ mg cm}^{-2}$) exhibit a higher rate capability in SL-based electrolytes.^[30] This could be ascribed to the significantly higher Li^+ transference number in the SL-based electrolytes, in which the fastest diffusion of Li^+ is enabled by a unique conduction mechanism based on Li-ion hopping/exchange with the chemical species in the electrolyte.^[30,31] Therefore, to further illustrate the effect of the high Li-ion transport capability of our electrolyte, we examined the Li–S coin cell behaviour using $[\text{Li}(\text{SL})_2][\text{NTf}_2] + 4.0\text{HFE}$ and a high sulfur loading (4.1 mg cm^{-2}) under the lean electrolyte condition ($80 \mu\text{L}$). As shown in Figure 5, even for the TiB-free cathode, a high discharge capacity of 1365 mAh g^{-1} was obtained with the $[\text{Li}(\text{SL})_2][\text{NTf}_2] + 4.0\text{HFE}$ electrolyte, which is significantly higher than that of the $[\text{Li}(\text{G4})_{0.8}][\text{NTf}_2] + 4.3\text{HFE}$ electrolyte. The surface morphologies of the TiB-free cathode discharged up to 250 mAh g^{-1} in the $[\text{Li}(\text{SL})_2][\text{NTf}_2] + 4.0\text{HFE}$ electrolyte were also obtained and compared with those of the cathodes discharged in the $[\text{Li}(\text{G4})_{0.8}][\text{NTf}_2] + 4.3\text{HFE}$ electrolyte (Figure 4a). The results of SEM combined with EDX sulfur mapping in Figure S5 are clearly different from the results presented in Figure 4(a); large crystal-like sulfur-containing particles were not observed for the cathodes discharged in the $[\text{Li}(\text{SL})_2][\text{NTf}_2] + 4.0\text{HFE}$ electrolyte. This distinctly different electrochemical behaviour can therefore be reasonably attributed to the intrinsic Li-ion transport

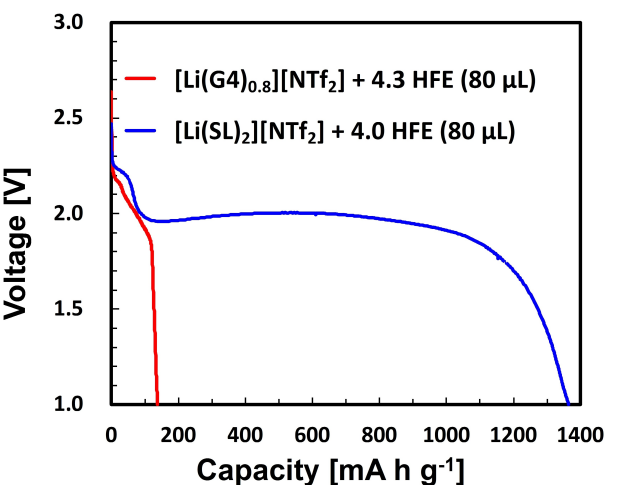


Figure 5. Discharge curves for the TiB-free cathode in $[\text{Li}(\text{G4})_{0.8}][\text{NTf}_2] + 4.3\text{HFE}$ (red line, S loading: 4.2 mg cm^{-2}) and in $[\text{Li}(\text{SL})_2][\text{NTf}_2] + 4.0\text{HFE}$ (blue line, S loading: 4.1 mg cm^{-2}) at $150 \mu\text{A cm}^{-2}$ under lean electrolyte conditions.

capability of the electrolytes.^[35] In addition to the intrinsic properties of the electrolyte, we also evaluated whether the TiB additive still enhanced the Li-ion transport in the $[\text{Li}(\text{SL})_2][\text{NTf}_2] + 4.0\text{HFE}$ electrolyte via GITT measurements (Figure S6). In the initial stage of the discharge process, the difference between the overpotentials of the TiB-free and TiB-added cathodes was not significant. However, upon increasing the depth of discharge, the difference in the overpotential gradually became significant. The smaller overpotential of the TiB-added cathode compared with that of the TiB-free cathode unequivocally suggests a smaller cell internal resistance owing to TiB addition. One possible reason for this result is that the Lewis acidity of the titanium atoms in TiB affects the adsorption, nucleation, and subsequent growth of the polysulfide and Li_2S species.^[41] In addition, the homogeneously distributed TiB contributes to the uniform growth of Li_2S , thereby affecting the porosity of the discharged cathode. Our previous study^[36] also demonstrated that sulfur cathodes show substantially different morphologies following the addition of TiB, especially after long-term cycling. The porosity loss of the sulfur cathode was extremely severe in the case of TiB-free cathodes, whereas it was maintained to a certain degree for the TiB-added electrodes. It is therefore reasonable to consider that the alleviation of the overpotential increase following the addition of TiB could be due to the facile Li-ion supply owing to the maintenance of the porosity of the TiB cathode.

Although GITT measurements can be used to separate the thermodynamic and kinetic factors, various kinetic factors that contribute to the overpotential, such as mass transport, charge transfer resistance, and iR drop, cannot be distinguished. Therefore, electrochemical impedance spectroscopy (EIS) was performed at various depths of discharge to separate the resistance components for further discussion. Nyquist plots obtained at various discharge depths corresponding to points A to F are shown in Figure S7 for the TiB-free and TiB-added cathodes. All

curves consisted of two depressed semicircles (the lower-frequency one was flattened) with an inclined spur. Figure S8 shows the Nyquist plot of a Li | [Li(SL)₂][NTf₂] + 4.0HFE | Li symmetrical cell in the frequency range of 1 MHz to 1 mHz. The high-frequency arc corresponds to the interfacial impedance between Li and the electrolyte, which may include contributions from the charge transfer resistance (R_{ct}) and solid-electrolyte interface resistance (R_{SE}). The low-frequency arc corresponds to the diffusion impedance in the electrolyte owing to the concentration polarisation of the salt. Comparison of the EIS data of the Li–S cells (Figure S7) with that of a Li||Li cell (Figure S8) reveals that the high-frequency arcs in the characteristic frequency range of 1–3 kHz in Figure S7 can be assigned to the interfacial impedance of the Li anode. Although the frequency ranges of the inclined spurs in Figure S7 and the low-frequency arc in Figure S8 are close, the impedance behaviour is completely different. This implies that the inclined spurs do not correspond to the diffusion process in the bulk electrolyte but to that in the cathode. The significantly depressed semicircles in the intermediate-frequency range may mainly correspond to the interfacial impedance of the S cathode.^[42,43] However, because we used composite cathodes consisting of S, KB, and binder polymers with or without TiB, it is difficult to discuss the EIS results of these composite cathodes in the Li–S batteries. In addition, the EIS features in the high- and intermediate-frequency ranges did not vary significantly in the presence or absence of TiB. The largest difference observed with the addition of TiB was in the low-frequency region, corresponding to the mass transport process in the cathode. Therefore, we focused on the Nyquist plot at point D (Figures S6 and S7, and 6), where the slope of the low-frequency EIS curve is close to 45°, corresponding to the diffusion impedance, and the EIS difference either in the presence or absence of TiB is the most apparent. This EIS feature is correlated with the Warburg impedance and is discussed in terms of the difference in the Warburg coefficients. The variation in Re (i.e., the real part of the impedance) as a function of $\omega^{-0.5}$ (i.e., the square root of the angular frequency)

for the TiB-free and TiB-added cathodes are shown in Figure 6(b), and the results were analysed according to Equations (1) and (2):

$$Re = R_{bulk} + R_{ct} + \sigma \cdot \omega^{-0.5}, \quad (1)$$

$$\sigma = \frac{RT}{n^2 F^2 A C} \cdot \frac{1}{\sqrt{2D_{Li}}}, \quad (2)$$

where σ is the Warburg coefficient, R is the gas constant, T is the absolute temperature, n is the number of transferred electrons, F is the Faraday constant, A is the area of the electrode, C is the concentration of the Li cation, and D_{Li} is the diffusion coefficient of the Li cation. As we employed composite cathodes, it was impossible to obtain the absolute values of the parameters, A , C , and D_{Li} in Equation (2). However, the smaller the value of σ is, the better the mass transport properties of a cathode is (larger A , C , and D_{Li}). If we assume that A and C are similar, irrespective of the addition of TiB, the smaller σ of the TiB-added cathode based on the slope of Figure 6(b) would suggest a faster diffusion of Li⁺ cations. This speculation is consistent with the previous discussion. Hence, the TiB additive not only improved the wettability of the sulfur cathode to the electrolyte but also accelerated a more homogeneous discharge reaction throughout the cathode, attributable to the improved maintenance of the porosity and enhanced Li⁺ ion transport.

Evaluation of the effects of TiB additive and electrolyte properties using a numerical simulation model

We employed a previously reported numerical simulation model of the Li–S cells with different electrolyte conditions to evaluate the effects of the TiB additive and electrolyte properties on the discharge performance.^[44–47] This model includes the reaction state of the polysulfide, mass transport of sulfide ions, and formation of solid Li₂S. The following assumptions were made in the simulation model:

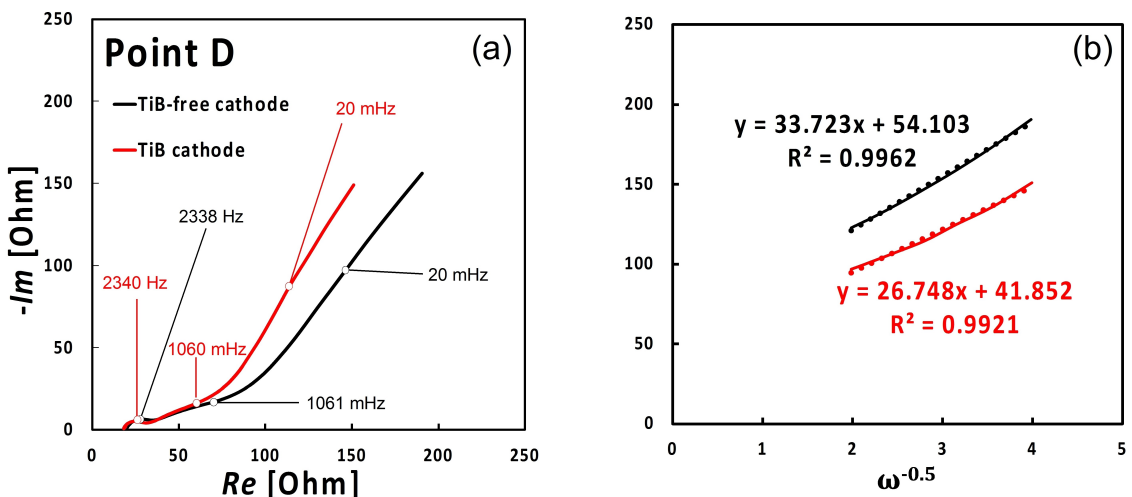


Figure 6. a) Nyquist plot obtained from EIS measurements at point D, and b) Re as function of $\omega^{-0.5}$.

- The porous structure in the cathode electrode layer is homogeneous;
- Heat loss due to an overvoltage can be neglected, and the temperature is constant and uniform;
- The dynamic stress distribution due to volume change of the active material is negligible;
- Side electrochemical reactions do not occur;
- The effect of the dissolution of solid sulfur and Li_2S_x is reflected in the increase in the volume of the electrolyte phase. Conversely, the effect of the deposition of solid Li_2S is reflected in the decrease in the volume of the electrolyte phase.

The Supporting Information of this paper provides the basic equations for the numerical simulation model (Table S1). In addition, Tables S2 and S3 show the electrode and separator conditions, respectively. In this study, we focused on the difference in the wettabilities of the cathodes^[36] to evaluate the effect of TiB. Considering that the porous electrode containing TiB was reported to have high wettability,^[36] it was assumed that the effect of TiB can be represented as an effective ion transfer network through the electrolyte phase in the porous electrode. Based on the Bruggeman equation, the effective ionic conductivity, σ^{eff} can be expressed as follows:

$$\sigma^{\text{eff}} = \sigma^{\text{bulk}} \varepsilon / \tau = \sigma^{\text{bulk}} \varepsilon^\gamma \quad (3)$$

where σ^{bulk} is the bulk ionic conductivity, ε is the porosity, τ is the tortuosity of the electrolyte phase in the porous electrode, and γ is the Bruggeman exponent. For the first simple evaluation, γ was set as 1.0 and 3.0 for the cathodes with and without TiB, respectively. As a result, the effective ionic conductivity was found to be higher in the TiB-added cathode than in that without TiB. Similarly, the effective diffusion coefficient of an ion can be expressed using the same approach. Moreover, to compare the effect of TiB in the presence of different electrolytes, $[\text{Li}(\text{G4})_{0.8}][\text{NTf}_2] + 4.3\text{HFE}$ and

$[\text{Li}(\text{SL})_2][\text{NTf}_2] + 4.0\text{HF}$, the electrolyte conditions were determined based on the data presented in Table S4. The Li diffusion coefficient, ionic conductivity, and transference number caused the most significant differences in mass transport. Additionally, the reaction constants of S_8 and Li_2S in each electrolyte were obtained by fitting the experimental data of charge/discharge. Thus, the effects of the electrode kinetics and mass transport properties of the electrolyte were evaluated through numerical simulations. The simulation was performed on the cathode and separator. The implicit Euler and finite difference methods were used for time and space discretisation, respectively. Furthermore, the successive over-relaxation method was used to solve the Poisson-type equations for quantities such as the concentration and potential. The relative error of the mass balance was set to $< 1\%$.

Figure 7 shows the simulation results of the discharge curve and the volume fractions of Li_2S in the cathodes with and without TiB. For the G4 electrolyte, the discharge performance in the TiB-added cathode was higher than that in the TiB-free cathode. This difference increased during the second discharge plateau. In contrast, the difference between the TiB-added and TiB-free electrodes was insignificant in the SL electrolyte. Moreover, the difference in both electrolytes appeared as a change in the volume fraction of the solid Li_2S . It should be noted that the discharge performance under each condition was not the same although the amount of Li_2S deposited in the cathode was the same.

Figure 8(a-d) shows the simulation results for the average concentrations of possible chemical species across the cathode during discharge, and Figure 8(e and f) shows the Li_2S volume fraction distribution at 250 mAh g^{-1} . The concentration of sulfide ions (S_x^{2-} : $x=8-1$) was varied sequentially. When the concentration of S^{2-} was $\sim 100 \text{ mol m}^{-3}$ (0.1 M), Li_2S was generated under both electrolyte conditions. As seen in Figure 8(e), for the TiB-free electrode in the G4 electrolyte, the volume fraction of $\text{Li}_2\text{S}(\text{s})$ is significantly large in the vicinity of

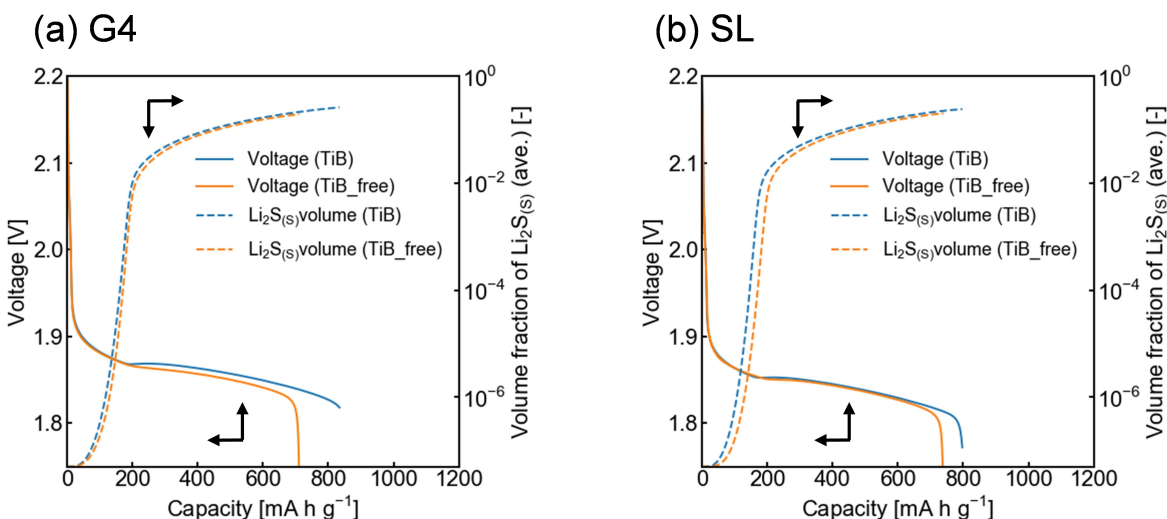


Figure 7. Simulation results for the discharge curves and Li_2S volume fractions in the cathodes with and without TiB in different electrolytes: a) $[\text{Li}(\text{G4})_{0.8}][\text{NTf}_2] + 4.3\text{HFE}$ and b) $[\text{Li}(\text{SL})_2][\text{NTf}_2] + 4.0\text{HF}$.

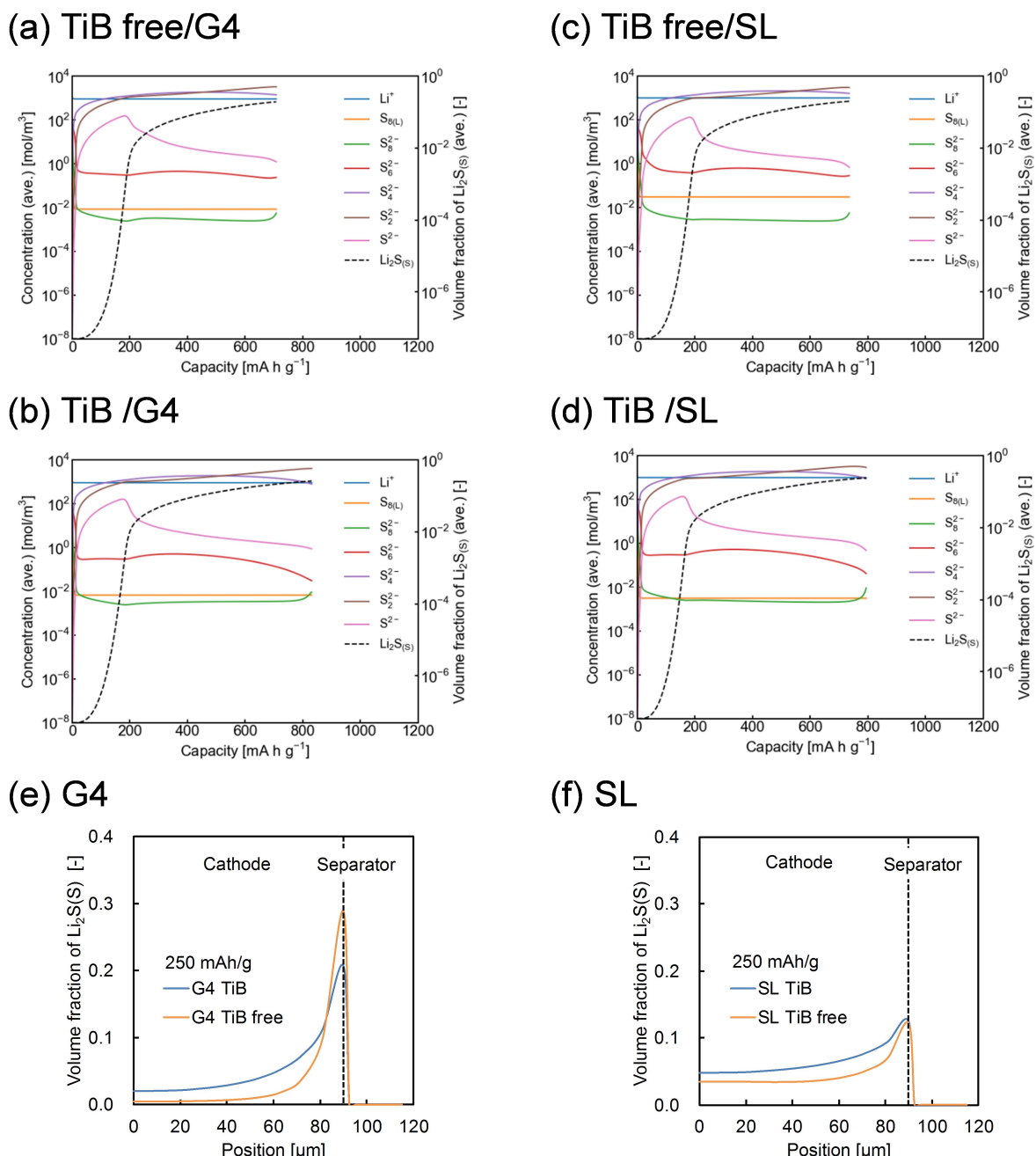


Figure 8. Simulation results for the average changes in the concentrations of the possible chemical species during the discharge of the electrode in a, b) electrolyte, c, d) SL electrolyte; a and c represent the results for the cathode without TiB, while b and d) represent the results for the cathode with TiB. Li₂S volume fraction distributions at 250 mAh/g for the two cathodes in the e) G4 electrolyte and f) SL electrolyte.

the separator, while being close to zero at the current corrector side. The inhomogeneous distribution of Li₂S(s) along the thickness direction of the electrode was less significant for the TiB-added electrode in the G4 electrolyte. In the SL electrolyte (Figure 8f), the TiB-added electrode exhibits a more homogeneous distribution of Li₂S(s), although the difference from the TiB-free electrode is small. These simulation results are qualitatively consistent with the experimental data presented in the former sections. Given the much lower Li transference number of the G4 electrolyte, a higher concentration gradient of the Li salt develops in the porous electrode, thereby

affecting the distribution of the Li₂S(s). Therefore, our simulations corroborate that Li₂S distribution strongly depends on the mass transport property of the electrolyte. The lower effective ionic conductivity and diffusion coefficient in the TiB-free electrodes was also represented well by the higher Bruggeman exponent and reproduced the localised deposition of Li₂S in the proximity of the separator, as observed in the SEM images (Figure 4a).

However, considering that this model was based on certain assumptions, a more detailed simulation model is required to include effects such as the dynamic structural change due to

volume expansion and the effect of morphological changes owing to the addition of TiB into the cathode.

Li–S pouch cell performance under lean electrolyte conditions

To evaluate the Li–S battery performance under extremely lean electrolyte conditions (low E/S), pouch-type cells, which have a low dead volume inside the cells, were fabricated. The structure of the pouch cell is shown in Figure S9. The sulfur loading was adjusted to $\sim 4.0 \text{ mg cm}^{-2}$, and the amount of electrolyte added to the pouch cell was $1500 \mu\text{L}$, corresponding to E/S values of 3.4–3.9 based on the electrolyte used. The charge/discharge curves are presented in Figure S10, and the cycle performance is shown in Figure 9. Consistent with the results of coin cells, an extremely low discharge capacity ($<200 \text{ mAh g}^{-1}$) was observed for the cell using TiB-free cathode and $[\text{Li}(\text{G4})_{0.8}][\text{NTf}_2] + 4.3\text{HFE}$. In contrast, the cell with the TiB-free cathode and $[\text{Li}(\text{SL})_2][\text{NTf}_2] + 4.0\text{HFE}$ electrolyte exhibited a high initial discharge capacity of 1133 mAh g^{-1} at a relatively high discharge rate of 0.1 C, and the discharge capacities were $>800 \text{ mAh g}^{-1}$ in the subsequent cycles. Moreover, pouch-type Li–S cells containing the TiB-added cathode and $[\text{Li}(\text{SL})_2][\text{NTf}_2] + 4.0\text{HFE}$ electrolyte with a higher sulfur loading (4.4 mg cm^{-2}) and thus a lower E/S value (3.4) were tested under harsh conditions. As shown in Figure 9, the initial discharge capacity was $>1200 \text{ mAh g}^{-1}$, and the discharge capacities were $>1000 \text{ mAh g}^{-1}$ in the subsequent cycles. Regarding the Coulombic efficiency, after the initial fluctuation for several cycles, the efficiency was almost 100% for the pouch cells using the SL-based electrolyte. For the cell using the G4-based electrolyte, it continued to decrease to 80% after 10 cycles. These results therefore indicate that the TiB additive was effective under the actual cell-operating conditions (i.e., a high sulfur loading and low E/S conditions) when pouch cells were employed.

Finally, we fabricated a large pouch-type Li–S cell with the structure shown in Figure 10. As shown in Figure 10(b), a high initial discharge capacity of 1382 mAh g^{-1} was obtained even under extremely lean electrolyte conditions (E/S = 3.0) and a relatively high sulfur loading (4.2 mg cm^{-2}), and the pouch cell delivered a high capacity of 1 Ah. Thus, a high energy density of 353 Wh kg^{-1} was successfully achieved (calculated based on the theoretical amount of lithium, excluding the weight of the Al laminate film and tabs). Thus, this work demonstrates Li–S cell operation under practical conditions, illustrating that changing the electrode structure as well as the electrolyte type has a significant impact on the Li–S cell performance.

Conclusion

In this study, we found that inhomogeneous discharge reactions could occur in Li–S cell cathodes under high sulfur loading (thick electrode) and lean electrolyte conditions that are essential for increasing the energy density. When the Li⁺ transport capability of the electrolyte was low [i.e., for a tetraglyme (G4)-based electrolyte], the discharge reactions of the sulfur cathode occurred preferentially at the surface of the cathode (i.e., close to the separator), and the discharge products blocked the void spaces at the surface. Moreover, the porosity of the cathode decreased owing to the expansion of the active material due to the conversion of S_8 to Li_2S_x . These changes inhibited the ion pathway to the inner regions of the electrode (i.e., close to the current collector) and inhibited further discharge reactions. In addition, the inclusion of TiB in the cathode could increase the wettability of the electrode to electrolytes, facilitating homogeneous discharge reactions throughout the cathodes. As a result, the porous structure of the cathode was maintained adequately, leading to significantly improved performance of the Li–S cell. Numerical simulations also supported the above consideration. Furthermore, combining the TiB additive with an electrolyte exhibiting

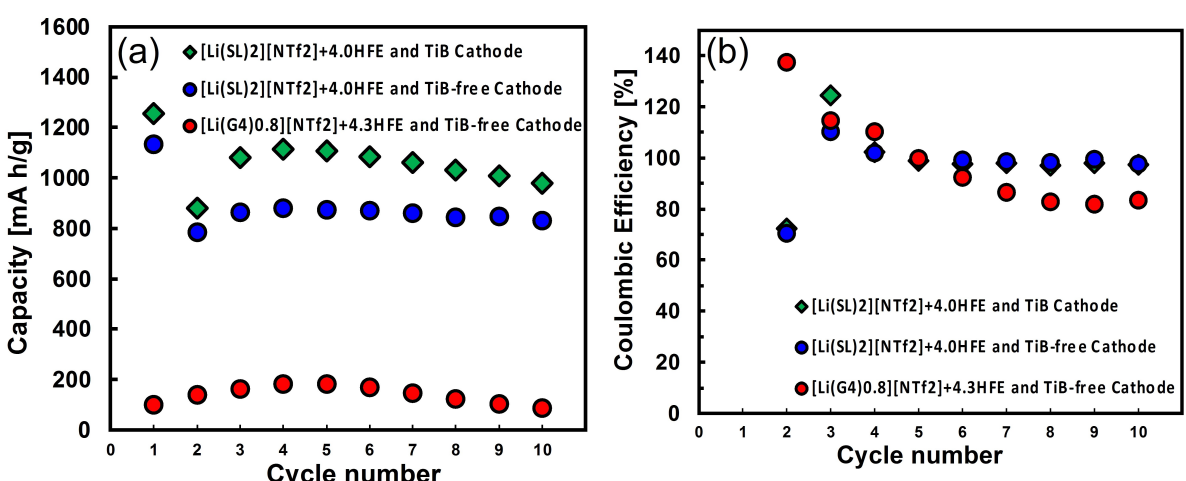


Figure 9. Discharge capacities a) and Coulombic efficiencies b) of the Li–S pouch cells at a current density of 0.1 C under high sulfur loading ($\sim 4.0 \text{ mg cm}^{-2}$) and lean electrolyte conditions [E/S = 3.4 (green diamonds), 3.9 (blue circles), and 3.8 (red circles)].

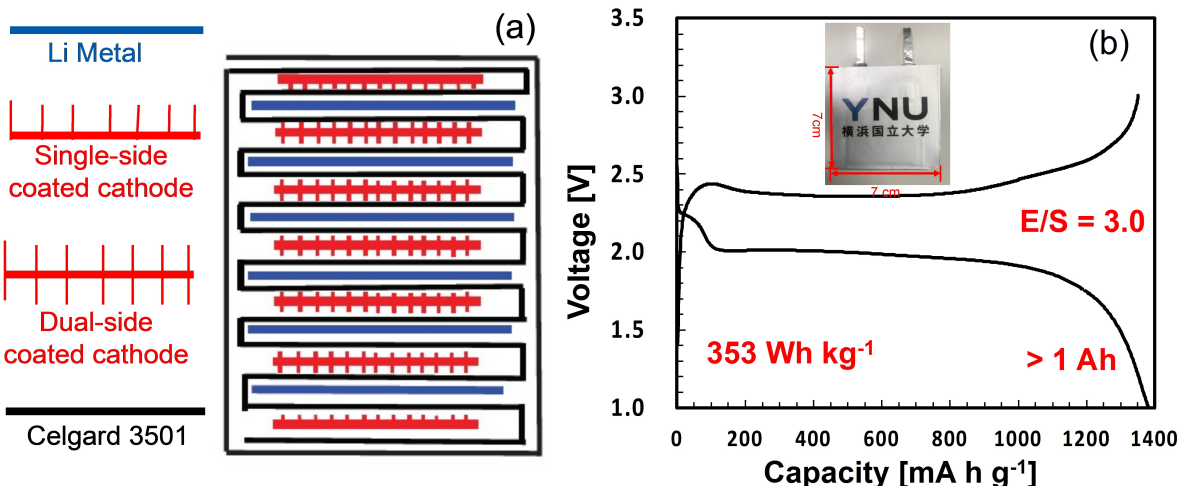


Figure 10. a) Illustration of the structure of a laminated Li–S pouch cell. b) Initial discharge ($137 \mu\text{A cm}^{-2}$, 0.02 C) and charge ($343 \mu\text{A cm}^{-2}$, 0.05 C) curves demonstrating an energy density of $> 350 \text{ Wh kg}^{-1}$ under high sulfur loading (4.2 mg cm^{-2}) and lean electrolyte (E/S = 3.0) conditions.

relatively high Li-ion transport capability [i.e., a sulfolane (SL)-based electrolyte] enabled a superior performance even under high sulfur loading and lean electrolyte conditions. Finally, a pouch cell fabricated with a sulfur loading of 4.2 mg cm^{-2} (E/S = 3.0) exhibited a high energy density of 353 Wh kg^{-1} . These results demonstrate the importance of mass transport in the cathode and electrolyte for improving the electrochemical performances of Li–S batteries.

Experimental Section

Preparation of the sulfur cathodes

A sulfur/carbon composite was prepared by the melt-diffusion method using a mixture of elemental sulfur (S_8 , Wako Chemical, Japan, 75 wt%) and porous carbon (Ketjen Black (KB), ECP600JD, Lion Corporation, Japan, 25 wt%). Given amounts of KB and S_8 were mixed using an agitating mortar, transferred to a sealable vial, and maintained at 155°C for 12 h to allow the diffusion of sulfur into the pores of the KB. The aqueous slurries for the electrode coating were prepared by mixing the S_8 /KB composite with carboxymethyl cellulose (CMC2200, Daicel FineChem, Japan) and styrene butadiene rubber (SBR, JSR Corporation, Japan) at a S_8 /KB:CMC2200:SBR weight ratio of 96.5:1.5:2. For comparison, TiB (Mitsubishi Material, Japan) was added to the slurry at a S_8 /KB:TiB:CMC2200:SBR weight ratio of 93.5:3:1.5:2. The obtained slurries with and without TiB were then coated onto carbon-coated aluminium foils as current collectors and dried in an oven at 60°C for 12 h to obtain the cathodes. The sulfur contents of the cathodes with and without TiB were 70.1 wt% and 72.3 wt%, respectively. Subsequently, the cathodes were cut into disc-shaped (for coin cells) or rectangular (for pouch cells) specimens, and dried in an oven under vacuum at 40°C for 12 h before use.

Preparation of the electrolytes

The electrolytes were prepared as reported earlier.^[35] More specifically, battery-grade Li[NTf₂] (Kishida Chemical, Japan) was mixed with purified G4 (Nippon Nyukazai, Japan) or SL (Kishida Chemical, Japan) in an Ar-filled glovebox at appropriate molar ratios to prepare

[Li(G4)_{0.8}][NTf₂] and [Li(SL)₂][NTf₂]. We selected the composition of [Li(G4)_{0.8}][NTf₂] instead of [Li(G4)₁][NTf₂] because it can provide superior rate capability, despite the low solubility of Li₂S_x in it.^[33] Subsequently, [Li(G4)_{0.8}][NTf₂] and [Li(SL)₂][NTf₂] were diluted with HFE (Daikin Industries, Japan) to obtain $\sim 1 \text{ M}$ Li[NTf₂] solutions. The compositions of the obtained homogeneous mixtures were [Li(G4)_{0.8}][NTf₂] + 4.3HFE and [Li(SL)₂][NTf₂] + 4.0HFE, respectively. The water contents in the electrolytes were $< 30 \text{ ppm}$, as determined by Karl Fisher titrations (CA-07, Mitsubishi Chemical, Japan).

Cell assembly

A 2032-type coin cell was assembled in an Ar-filled glove box using either the TiB-added cathode or TiB-free cathode (14 mm diameter), a Li metal anode (Honjo Metal, 16 mm diameter), two pieces of Celgard 3501 separator, and an electrolyte volume of either 80 or 110 μL , denoted as lean or sufficient electrolyte conditions, respectively. Pouch cells were fabricated using a layer-by-layer process to laminate the cathode (coating of either one or both sides of a carbon-coated Al current collector, 45 \times 37 mm), Celgard 3501 separator (50 \times 43 mm), and anode (50 \times 40 mm). Li metal coated on both sides of Cu foil (Li thickness = 90 μm , Honjo Metal, Japan) was used as the anode. The charge/discharge measurements were performed on a charge-discharge tester (HJ1001SD8, Hokuto Denko, Japan) at 30°C using a current density of $150 \mu\text{A cm}^{-2}$ and cut-off potentials of 1.0 and 3.0 V for the discharge and charge steps, respectively. GITT measurements (VMP3, Bio-Logic, France) were performed with constant discharge currents of 150 and $375 \mu\text{A cm}^{-2}$ for the [Li(G4)_{0.8}][NTf₂] + 4.3HFE and [Li(SL)₂][NTf₂] + 4.0HFE electrolytes, respectively. The discharge time was set to 1 h (Figure 2) or 3 h (Figure S6) for each pulse, and the relaxation time between pulses was set to reach a time-dependent cell voltage variation of $< 15.0 \text{ mV h}^{-1}$. After the GITT measurements, which were carried out to achieve a certain depth of discharge, and subsequent relaxing of the cell potential to the equilibrium state (potential variation: $< 15.0 \text{ mV h}^{-1}$), EIS was performed on a VMP3 instrument (Bio-Logic, France) in the frequency range of 500 kHz to 10 mHz with a sinusoidal voltage amplitude of 10 mV.

Characterization

To study the electrochemical products formed on the sulfur cathodes during cycling, the cells were disassembled in an Ar-filled glove box. The sulfur cathodes were separated and rinsed several times with pure HFE to remove the electrolyte residue. The cathodes were maintained under an inert atmosphere during the sample preparation and transfer to the testing instruments. SEM with EDX was performed on a Hitachi FE-SEM SU8000 instrument (Japan) to observe the morphologies of the electrodes and obtain elemental maps.

Acknowledgements

This work was supported by the Japan Science and Technology Agency (JST) ALCA-SPRING, Japan (Grant No. JPMJAL1301). We would like to thank Editage (www.editage.com) for English language editing.

Conflict of Interest

The authors declare no conflict of interest.

Data Availability Statement

The data that support the findings of this study are available on request from the corresponding author. The data are not publicly available due to privacy or ethical restrictions.

Keywords: concentrated electrolyte • Li–S battery • mass transport • numerical simulation • sparingly solvating electrolyte

- [1] J. B. Goodenough, *Acc. Chem. Res.* **2013**, *46*, 1053–1061.
- [2] B. Dunn, H. Kamath, J. M. Tarascon, *Science* **2011**, *334*, 928–935.
- [3] J. M. Tarascon, *Philos. Trans. R. Soc. London Ser. A* **2010**, *368*, 3227–3241.
- [4] D. Larcher, J. M. Tarascon, *Nat. Chem.* **2015**, *7*, 19–29.
- [5] J. B. Goodenough, K. S. Park, *J. Am. Chem. Soc.* **2013**, *135*, 1167–1176.
- [6] N. S. Choi, Z. Chen, S. A. Freunberger, X. Ji, Y. K. Sun, K. Amine, G. Yushin, L. F. Nazar, J. Cho, P. G. Bruce, *Angew. Chem. Int. Ed.* **2012**, *51*, 9994–10024; *Angew. Chem.* **2012**, *124*, 10134–10166.
- [7] A. Manthiram, Y. Fu, S. H. Chung, C. Zu, Y. S. Su, *Chem. Rev.* **2014**, *114*, 11751–11787.
- [8] P. G. Bruce, S. A. Freunberger, L. J. Hardwick, J. M. Tarascon, *Nat. Mater.* **2012**, *397*, 19–29.
- [9] D. Bresser, S. Passerini, B. Scrosati, *Chem. Commun.* **2013**, *49*, 10545–10562.
- [10] A. Manthiram, Y. Fu, Y. S. Su, *Acc. Chem. Res.* **2012**, *46*, 1125–1134.
- [11] W. J. Chung, J. J. Griebel, E. T. Kim, H. Yoon, A. G. Simmonds, H. J. Ji, P. T. Dirlam, R. S. Glass, J. J. Wie, N. A. Nguyen, B. W. Guranlnick, J. Park, A. Somogyi, P. Theato, M. E. Mackay, Y. E. Sung, K. Char, J. Pyun, *Nat. Chem.* **2013**, *5*, 518–524.
- [12] X. Ji, L. F. Nazar, *J. Mater. Chem.* **2013**, *404*, 9821–9826.
- [13] F. Y. Fan, Y.-M. Chiang, *J. Electrochem. Soc.* **2017**, *164*, A917–A922.
- [14] M. Hagen, P. Fanz, J. Tubke, *J. Power Sources* **2014**, *264*, 30–34.
- [15] D. Eroglu, K. R. Zavadil, K. G. Gallagher, *J. Electrochem. Soc.* **2015**, *162*, A982–A990.
- [16] P. Bonnick, E. Nagai, J. Muldoon, *J. Electrochem. Soc.* **2018**, *165*, A6005–A6007.
- [17] L. Cheng, L. A. Curtiss, K. R. Zavadil, A. A. Gewirth, Y. Shao, K. G. Gallagher, *ACS Energy Lett.* **2016**, *1*, 503–509.
- [18] C. W. Lee, Q. Pang, S. Ha, L. Cheng, S. D. Han, K. R. Zavadil, K. G. Gallagher, L. F. Nazar, M. Balasubramanian, *ACS Cent. Sci.* **2017**, *3*, 6056–613.
- [19] L. X. Yuan, J. K. Feng, X. P. Ai, Y. L. Cao, S. L. Chen, H. X. Yang, *Electrochim. Commun.* **2006**, *8*, 610–614.
- [20] N. Tachikawa, K. Yamauchi, E. Takashima, J. W. Park, K. Dokko, M. Watanabe, *Chem. Commun.* **2011**, *47*, 8157–9159.
- [21] J. W. Park, K. Ueno, N. Tachikawa, K. Dokko, M. Watanabe, *J. Phys. Chem. C* **2013**, *117*, 20531–20541.
- [22] L. M. Suo, Y. S. Hu, H. Li, M. Armand, L. Q. Chen, *Nat. Commun.* **2013**, *4*, 1481.
- [23] E. S. Shin, K. Kim, S. H. Oh, W. Il Cho, *Chem. Commun.* **2013**, *49*, 2004–2006.
- [24] N. Azimi, W. Weng, C. Takoudis, Z. Zhang, *Electrochim. Commun.* **2013**, *37*, 96–99.
- [25] S. D. Taliani, S. Jeschke, A. Vizintin, K. Pirnat, I. Arcon, G. Aquilanti, P. Johansson, R. Dominko, *Chem. Mater.* **2017**, *29*, 10037–10044.
- [26] M. Cuisinier, P.-E. Cabelguen, B. D. Adams, A. Garsuch, M. Balasubramanian, L. F. Nazar, *Energy Environ. Sci.* **2014**, *7*, 2697–2705.
- [27] C.-C. Su, M. He, R. Amine, K. Amine, *Angew. Chem. Int. Ed.* **2019**, *58*, 10591–10595; *Angew. Chem.* **2019**, *131*, 10701–10705.
- [28] K. Ueno, R. Tataria, S. Tsuzuki, S. Saito, H. Doi, K. Yoshida, T. Mandai, M. Matsugami, Y. Umebayashi, K. Dokko, M. Watanabe, *Phys. Chem. Chem. Phys.* **2015**, *17*, 8248–8257.
- [29] K. Dokko, N. Tachikawa, K. Yamauchi, M. Tsuchiya, A. Yamazaki, E. Takashima, J. W. Park, K. Ueno, S. Seki, N. Serizawa, M. Watanabe, *J. Electrochem. Soc.* **2013**, *160*, A1304–A1310.
- [30] A. Nakanishi, K. Ueno, D. Watanabe, Y. Ugata, Y. Matsumae, J. Liu, M. L. Thomas, K. Dokko, M. Watanabe, *J. Phys. Chem. C* **2019**, *123*, 14229–14238.
- [31] K. Dokko, D. Watanabe, Y. Ugata, M. L. Thomas, S. Tsuzuki, W. Shinoda, K. Hashimoto, K. Ueno, Y. Umebayashi, M. Watanabe, *J. Phys. Chem. B* **2018**, *122*, 10736–10745.
- [32] C. Weller, S. Thieme, P. Härtel, H. Althues, S. Kaskel, *J. Electrochem. Soc.* **2017**, *164*, A3766–A3771.
- [33] P. Strubel, S. Thieme, C. Weller, H. Althues, S. Kaskel, *Nano Energy* **2017**, *34*, 437–441.
- [34] M. Hagen, D. Hanselmann, K. Ahlbrecht, R. Maca, D. Gerber, J. Tubke, *Adv. Energy Mater.* **2015**, *5*, 1401986.
- [35] M. Yanagi, K. Ueno, A. Ando, S. Li, Y. Matsumae, J. Liu, K. Dokko, M. Watanabe, *J. Electrochem. Soc.* **2020**, *167*, 070531.
- [36] J. Liu, S. Li, M. Marium, B. Wang, K. Ueno, K. Dokko, M. Watanabe, *Sustain. Energy Fuels* **2021**, *5*, 1821–1831.
- [37] M. Zhao, B. Q. Li, H. J. Peng, H. Yuan, J. Y. Wei, J. Q. Huang, *Angew. Chem. Int. Ed.* **2020**, *59*, 12636–12652; *Angew. Chem.* **2020**, *132*, 12736–12753.
- [38] J. Chen, W. A. Henderson, H. Pan, B. R. Perdue, R. Cao, J. Z. Hu, C. Wan, K. S. Han, K. T. Mueller, J.-G. Zhang, Y. Shao, J. Liu, *Nano Lett.* **2017**, *17*, 3061–3067.
- [39] C. Luo, E. Hu, K. J. Gaskell, X. Fan, T. Gao, C. Cui, S. Ghose, X.-Q. Yang, C. Wang, *Proc. Natl. Acad. Sci. USA* **2020**, *117*, 14712–14720.
- [40] A. Bhargav, J. He, A. Gupta, A. Manthiram, *Joule* **2020**, *4*, 285–291.
- [41] Q. Pang, D. Kundu, M. Cuisinier, L. F. Nazar, *Nat. Commun.* **2014**, *5*, 4759.
- [42] L. Wang, J. Zhao, X. He, C. Wan, *Electrochim. Acta* **2011**, *56*, 5252–5256.
- [43] J. Yan, X. Liu, B. Li, *Adv. Sci.* **2016**, *3*, 1600101.
- [44] K. Kumaresan, Y. Mikhaylik, R. E. White, *J. Electrochem. Soc.* **2008**, *155*, A576.
- [45] M. Ghaznavi, P. Chen, *J. Power Sources* **2014**, *257*, 394–401.
- [46] K. Yoo, M. K. Song, E. J. Cairns, P. Dutta, *Electrochim. Acta* **2016**, *213*, 174–185.
- [47] T. Danner, G. Zhu, A. F. Hofmann, A. Latz, *Electrochim. Acta* **2015**, *184*, 124–133.

Manuscript received: December 23, 2021

Revised manuscript received: February 4, 2022

Version of record online: March 1, 2022